

# A Numerical Study of the Evolving Convective Boundary Layer and Orographic Circulation around the Santa Catalina Mountains in Arizona. Part I: Circulation without Deep Convection

J. CORY DEMKO AND BART GEERTS

*University of Wyoming, Laramie, Wyoming*

(Manuscript received 15 June 2009, in final form 22 September 2009)

## ABSTRACT

The daytime evolution of the thermally forced boundary layer (BL) circulation over an isolated mountain, about 30 km in diameter and 2 km high, is examined by means of numerical simulations validated with data collected in the Cumulus Photogrammetric, In Situ, and Doppler Observations (CuPIDO) field campaign. Two cases are presented, one remains cloud free in the simulations, and the second produces orographic convection just deep enough to yield a trace of precipitation. The Weather Research and Forecasting version 3 simulations, at a resolution of 1 km, compare well with CuPIDO observations.

The simulations reveal a solenoidal circulation mostly contained within the convective BL, but this circulation and especially its upper-level return flow branch are not immediately apparent since they are overwhelmed by BL thermals. A warm anomaly forms over the high terrain during the day, but it is rather shallow and does not extend over the depth of the convective BL, which bulges over the mountain. Low-level mountain-scale convergence (MSC), driven by an anabatic pressure gradient, deepens during the day. Even relatively shallow and relatively small cumulus convection can temporarily overwhelm surface MSC by cloud shading and convective downdraft dynamics. In the evening drainage flow develops near the surface before the anabatic forcing ceases, and anabatic flow is still present in the residual mixed layer, decoupled from the surface. The interaction of the boundary layer circulation with deep orographic convection is examined in Part II of this study.

## 1. Introduction

During the summer, cumulus convection erupts almost daily close to solar noon over the mountain ranges of the interior western United States (e.g., Banta and Schaaf 1987). This moist convection typically grows in a deep, weakly capped convective boundary layer (CBL) under weak winds. It is essential to warm-season precipitation and to surface–troposphere exchange of water and heat in the region. Even relatively simple numerical simulations have shown that under sufficient surface heating, weak stratification, and weak wind, a thermally direct circulation develops over a mountain, with anabatic flow converging over a mountain (e.g., Orville 1964). It is generally believed that the low-level convergence associated with this toroidal circulation, combined with heating over elevated terrain, is responsible for the initiation

and maintenance of cumulus convection over or near the mountain [e.g., Fig. 8.15 in Whiteman (2000)].

Few observational studies have documented the thermally forced toroidal circulation over mountains, and they generally only describe the surface component (e.g., Fujita et al. 1962; Garrett 1980; Banta 1984; Vergeiner and Dreiseitl 1987; Hernández et al. 1998). Demko et al. (2009) used both aircraft and surface measurements to characterize this circulation around the relatively isolated Santa Catalina Mountains (CM) in Arizona, a mountain range peaking ~2000 m above the surrounding plains with a diameter of ~30 km. The surface measurements around the CM clearly reveal the diurnal evolution of mountain-scale convergence (MSC), which tends to peak around solar noon (Demko et al. 2009). The divergent component of the toroidal circulation near the CBL top proved more difficult to capture using aircraft data, even with ~50 flight loops around the CM. Surface measurements around and on top of the CM show that the MSC is forced by a diurnally varying horizontal perturbation pressure difference between the high terrain and the surrounding plains (Geerts et al.

---

*Corresponding author address:* J. Cory Demko, Department of Atmospheric Sciences, University of Wyoming, Laramie, WY 82071.

E-mail: coryuw@uwyo.edu

2008). The diurnal signal of this perturbation pressure difference suggests that is due to heating of the CBL over elevated terrain.

Because the mountains that drive the CBL convergence and deep convection are generally small compared to model resolution, the resulting cloudiness and precipitation are poorly predicted by current-generation numerical weather prediction (NWP) models (e.g., Davis et al. 2003; Yuan et al. 2007). Even NWP model simulations of sufficient resolution to resolve the thermally direct orographic circulations are challenged in their ability to simulate the surface fluxes and CBL growth over complex terrain, and thus to accurately predict the timing and intensity of ensuing thunderstorms (e.g., Trentmann et al. 2009). Several modeling studies have depicted the development of the daytime CBL around a mountain, and the ensuing thermally forced circulations, but most studies have assumed an idealized vertical profile and an idealized mountain (e.g., Kimura and Kuwagata 1993; Reisner and Smolarkiewicz 1994; De Wekker et al. 1998; Crook and Tucker 2005; De Wekker 2008), or they assumed a much larger mountain range than the CM (e.g., Paegle and McLawhorn 1983; Zhang and Koch 2000; Koch et al. 2001).

This paper employs real cases to simulate CBL development over a real mountain range (i.e., the CM). The selected cases come from the Cumulus Photogrammetric, In Situ, and Doppler Observations (CuPIDO) field campaign (Damiani et al. 2008), which generated detailed observations essential for basic model validation. This paper first verifies whether the model captures the observed surface MSC and its forcing. The objective of this paper then is to use the spatially and temporally continuous, dynamically consistent model output to shed light upon the nature and dynamics of CBL growth and orographic circulations. This paper is the first part of a two-part study; it focuses on cases with at most mediocre cumulus convection over the CM, of insufficient depth to produce a significant cold pool. It sets the stage for Part II (J. C. Demko and B. Geerts 2009, unpublished manuscript), which focuses on the interaction between CBL flow and orographic deep convection.

Section 2 describes the numerical model along with data sources used. Section 3 describes two case studies, first a cloud-free event, and then a case with simulated Cu mediocris over the mountain. The results are discussed in section 4.

## 2. Numerical model setup and data sources

Numerical simulations using the Weather Research and Forecasting Nonhydrostatic Mesoscale Model (WRF-NMM) model version 3.0.1.1 have been conducted on

TABLE 1. Configuration of the WRF model used for the simulations in this study. Multiple values separated by commas indicate domains 1 through 3, respectively (Fig. 1). (Information about the schemes listed can be found online at <http://www.dtcenter.org/wrf-nmm/users/>.)

Horizontal grid resolution (km)	9, 3, 1
No. of vertical levels	43, 43, 43
Microphysics	Lin et al. (1983) scheme
Longwave radiation	Rapid Radiative Transfer Model
Shortwave radiation	Dudhia scheme
Surface layer	Eta similarity
Land surface	Noah land surface model
Planetary boundary layer	Mellor–Yamada–Janjić scheme
Cumulus parameterization	Kain–Fritsch scheme, none, none

several days during CuPIDO. The simulation architecture including domains, resolution, and physics options is summarized in Table 1. A triple nesting is used; each model domain is centered on the CM range (Fig. 1) and interacts with the other domains in both directions. This study presents results from the inner domain (1-km resolution) only. Test simulations at both coarser and finer resolutions suggest that 1 km is just sufficient to capture the essential elements of the flow over the CM, including MSC and cumulus convection. The vertical coordinate is terrain following (sigma coordinates) with 43 levels. The surface energy balance calculation in WRF version 3 includes the effects of terrain slope and orientation. Soil temperature and moisture are computed using the Noah land surface model, with initial values determined by the 12-km North American Mesoscale (NAM) grids. These grids are used for all initial and boundary conditions.

The WRF simulations presented herein use the Mellor–Yamada–Janjić (MYJ) scheme for the parameterization of planetary boundary layer (PBL) processes (Table 1). Model output using three different PBL schemes was compared with ISFF observations. The three schemes differ little in terms of the evolution of integrated anabatic flow (MSC): the time of transition from katabatic to anabatic flow was the same within an hour, and the peak surface MSC values were within 15% of each other. Simulations start at 0000 UTC (1700 LT, i.e., in the evening before the day of interest). The period from 0600 UTC (0100 LT–run date) to 0600 UTC (0100 LT–following day) is analyzed, to capture the full diurnal cycle. The model output is analyzed at the surface and on isobaric surfaces with data interpolated from the sigma levels.

The CuPIDO experimental data (Damiani et al. 2008) are used for validation only. Ten Integrated Surface Flux Facility (ISFF) platforms collected meteorological variables around the mountain (Fig. 2).

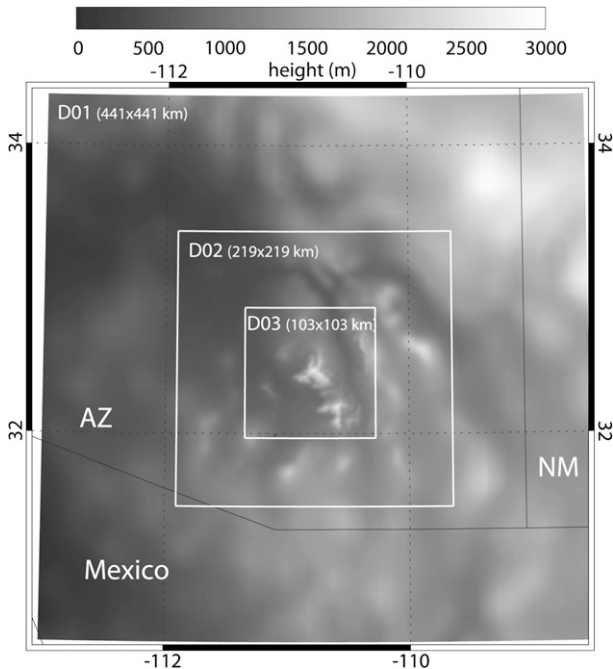


FIG. 1. The three domains of the nested WRF simulations. The Santa Catalina Mountains are in the center of the inner domain. The terrain is gray shaded at the resolution of each domain.

**3. WRF simulations of individual cases**

We select two CuPIDO cases to examine the development of the CBL and anabatic flow around the CM.

The cases, 12 and 9 July 2006, are chosen for three reasons: no precipitation was measured by any of the 10 ISFF stations, no lightning occurred within 13 km of Mt. Lemmon according to the National Lightning Detection Network (NLDN) data, and at most cumulus mediocris formed over the CM, as recorded by cameras around the mountain.

*a. 12 July 2006: A case without simulated orographic cumulus*

1) MODEL VALIDATION

The predawn (1200 UTC) Tucson, Arizona (KTUS), sounding on 12 July suggests very little nocturnal cooling near the ground (Fig. 3). The most unstable CAPE ( $302 \text{ J kg}^{-1}$ ) in this sounding applies to a parcel lifted from the surface. The low-level air mass is relatively dry, with a lifting condensation level (LCL) at 722 hPa. The WRF 1200 UTC sounding corresponds well with the KTUS sounding, but it is slightly drier than observed below 675 hPa, and thus the WRF simulation lacks the observed CAPE and low-level potential instability. Both the observed and the modeled wind profiles exhibit very weak flow from the surface to  $\sim 450$  hPa, mostly northwesterly below the mountain top (2791 m or  $\sim 730$  hPa) and southerly above this level.

On this day high-cloud-base, shallow orographic cumulus (Cu) convection developed, starting 1 h before solar noon (1929 UTC), and becoming Cu congestus for

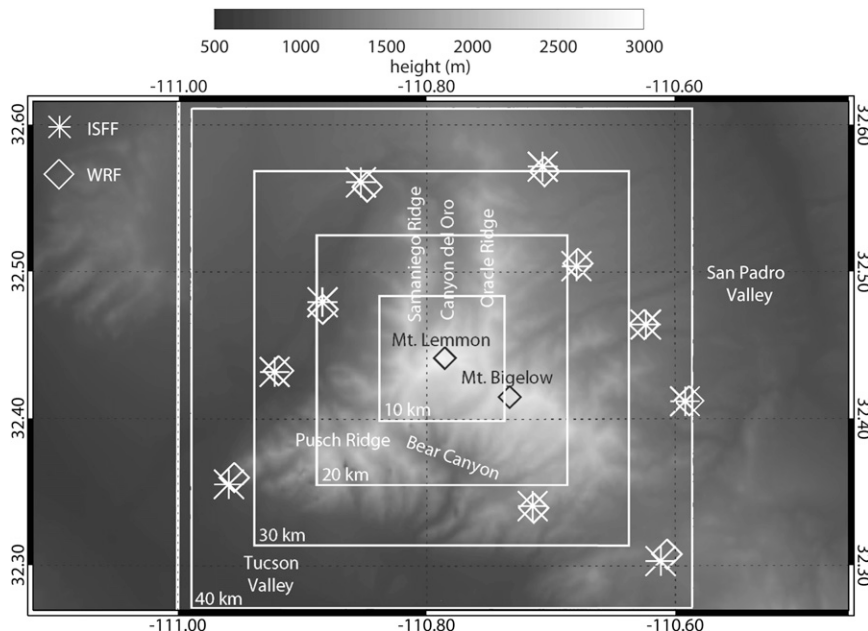


FIG. 2. Close-up of the inner domain showing the terrain (gray shading), the location of the 10 ISFF stations and their closest grid points, the square boxes used for MSC calculations, and several geographic markers.

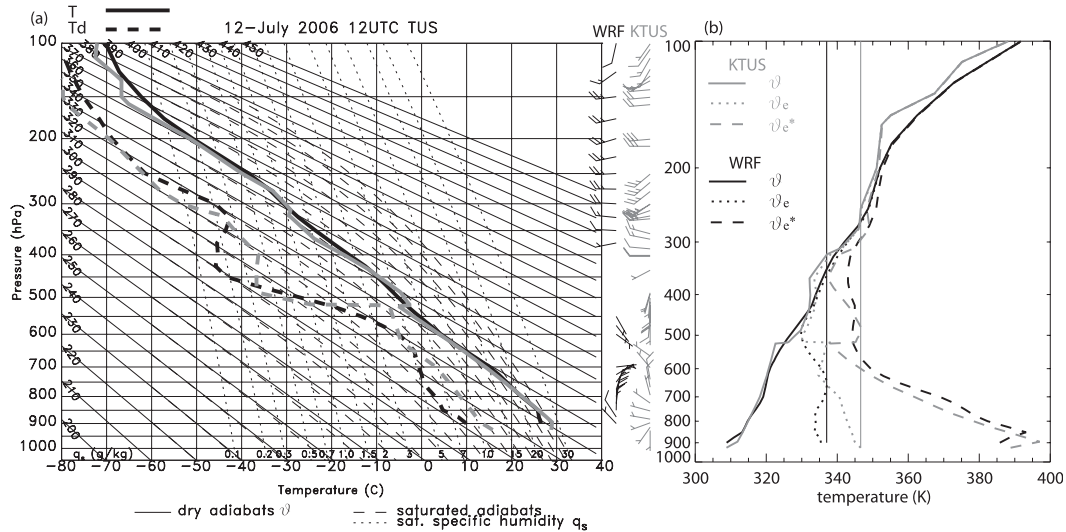


FIG. 3. (a) KTUS sounding at 1200 UTC 12 Jul 2006 observed (gray lines and wind barbs) and model (black) soundings both with wind profiles on the right (full barb = 10 kt); (b) corresponding profiles of potential temperature  $\theta$ , equivalent potential temperature  $\theta_e$ , and saturated equivalent potential temperature  $\theta_e^*$ . The vertical line carries  $\theta_e$  from the most unstable level near the surface upward, indicating the amount of CAPE in the environment.

3 h in the early afternoon, with a maximum cloud depth of 5.1 km (Fig. 4a). Clouds first formed over the highest peak and later mainly over Bigelow ridge (Fig. 4b). The cloud data in Fig. 4 are based on stereo-photogrammetric analysis (Zehnder et al. 2007), yielding the 3D geolocation of the highest Cu in a  $30 \times 30 \text{ km}^2$  box centered on Mt. Lemmon. No precipitation virga could be seen in the camera footage. WRF does not resolve any orographic clouds on this day, at least not with the default model setup (section 2). A slight amount of CAPE ( $<100 \text{ J kg}^{-1}$ ) does develop over the mountain, but cumulus convection is hindered by a similar amount of convective inhibition (CIN; Fig. 4a). The model CAPE

vanishes in the early afternoon, as the CBL deepens, mixing down very dry air. The PBL height, shown in Fig. 4a, is a model-defined variable; it corresponds with the CBL height during the daytime.

The diurnal temperature trend observed at the 10 ISFF stations around the mountain and one on the mountain top (Fig. 2) is captured well by WRF (Fig. 5), although the model generates surface temperatures  $\sim 2 \text{ K}$  warmer than observed between 1700 and 2300 UTC. The model accurately captures an east–west gradient, the west side stations being cooler by 1–2 K, mainly around sunrise (because several west-side stations are in local valleys) and persisting throughout the day, suggesting east–west

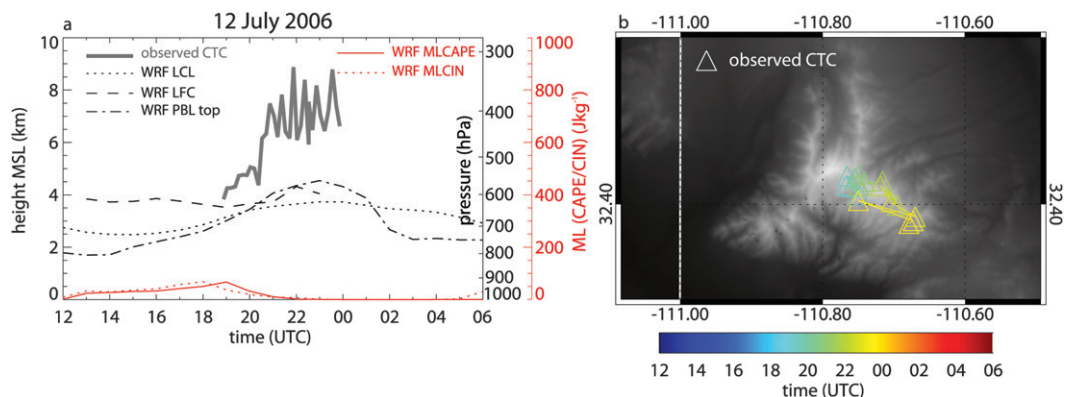


FIG. 4. Trend of observed vs modeled orographic cumulus top evolution. (a) Cloud-top chronology (CTC) and (b) location of the highest cloud top. The time resolution is 20 min for the observations and hourly for the model output. (a) The trend of various stability parameters, computed from model output within the  $30 \times 30 \text{ km}^2$  box. [Note: mixed-layer CAPE (MLCAPE) and mixed-layer convective inhibition (MLCIN).]

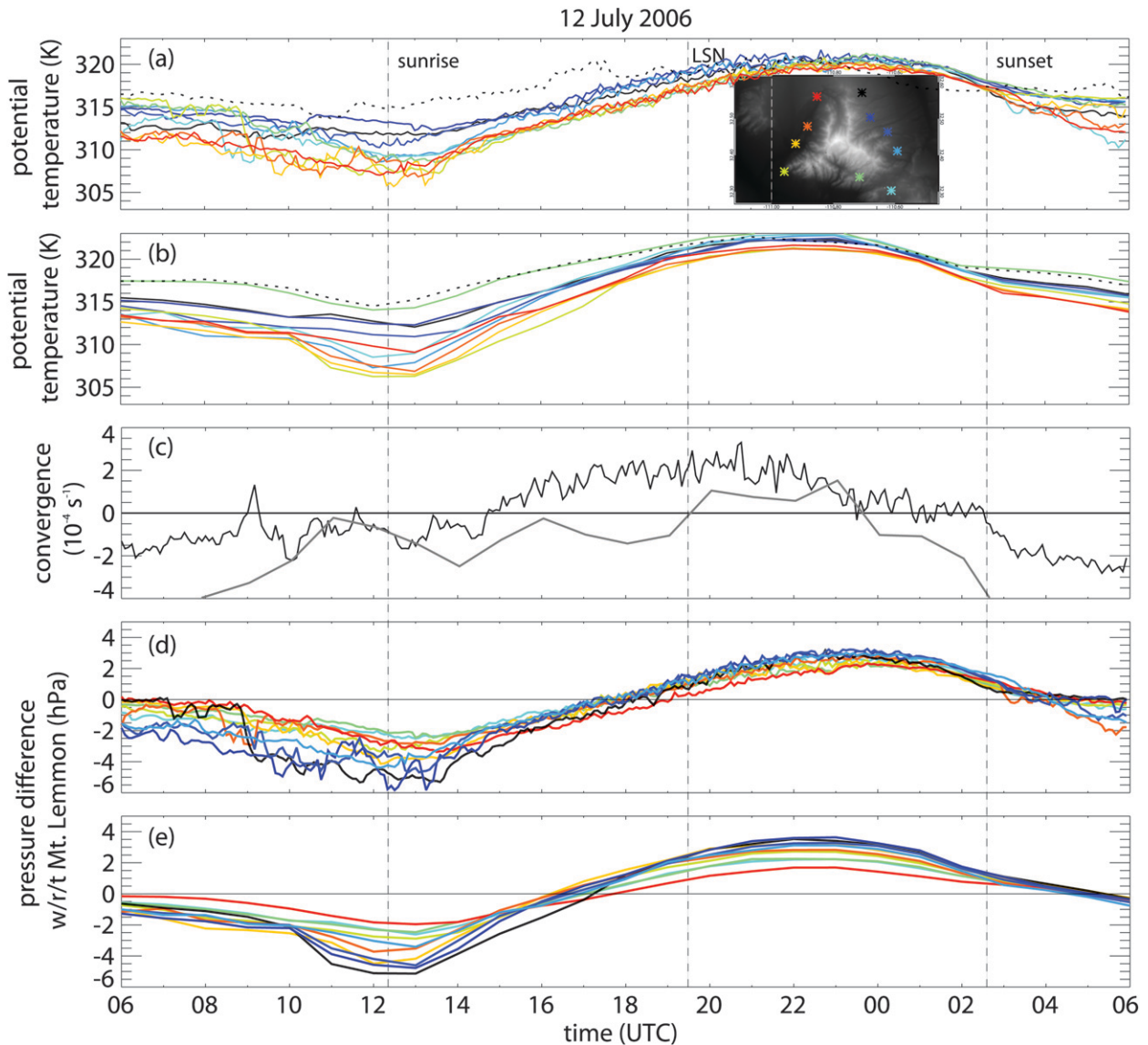


FIG. 5. Trend of observed vs WRF-simulated variables on 12 Jul 2006. The vertical dashed lines indicate the times of sunrise, local solar noon (LSN), and sunset. (a) Observed potential temperature at Mt. Bigelow (dashed black line) and at the ISFF stations color coded as shown in the insert terrain map; (b) as in (a), but modeled; (c) observed (black) and modeled (gray) surface MSC calculated from the 10 ISFF stations and WRF's closest grid point; (d) observed horizontal perturbation pressure difference between the ISFF stations and the mountain top (positive values imply a lower pressure over the mountain); and (e) as in (d), but modeled.

differences in surface energy balance. At night the observed and simulated mountain top potential temperature exceeds that at the foothills, typical for a stably stratified atmosphere. As the CBL grows above the mountaintop (between 1800 and 1900 UTC in the model, Fig. 4a), that difference largely, but not entirely, vanishes. Thus, the WRF surface data suggest some solenoidal forcing (i.e., an anomalously warm CBL over the mountain), mainly in the late morning hours. In the late afternoon (2300–0000 UTC) the observed mountaintop potential temperature became slightly less than at lower

elevations (Fig. 5a), suggesting a shutoff of any solenoidal forcing. Cumulus convection also ceased at this time (Fig. 4a).

Mountain-scale convergence (Fig. 5c) is computed as a finite-line integral of flow toward the mountain, normal to the polygon composed of midpoints between ISFF stations [see Demko et al. (2009) for details]. The trend of observed surface MSC (Fig. 5c) is broadly consistent with the solenoidal forcing, with convergence starting about 2 h after sunrise and peaking near solar noon. This is rather typical for the CM in summer (Geerts

et al. 2008). On 12 July the surface MSC essentially vanished in the afternoon about the time ( $\sim 2330$  UTC) that the mountain-top potential temperature became lower than elsewhere (Fig. 5a). The model MSC calculated from 10 matching grid points (Fig. 2) is mostly negative (net katabatic flow) and only briefly becomes positive at 2000 UTC, just after solar noon (Fig. 5c). Yet it remains to be seen whether the 10-point MSC calculation is representative (i.e., whether 10 points are enough to capture the integrated flow within a closed loop encompassing the mountain). For instance, the orange and red stations on the northwest side (Fig. 5a) are in a local valley (Oro Valley) that drains to the south, thus drainage flow would have an “anabatic” (toward Mt. Lemmon) component. Below we will compute model MSC from a loop integral at the model’s resolution (1 km).

The pressure gradient forcing is less sensitive to local terrain because hydrostatic pressure is an integral quantity affected by the temperature profile. Wind and nonhydrostatic pressure perturbations (e.g., due to cumulus convection) can make the pressure field quite sensitive to the details of the terrain, but both were weak on this day. It is generally accepted that daytime surface anabatic flow and MSC are part of a solenoidal circulation driven by a low pressure anomaly (heat low) over elevated terrain. Geerts et al. (2008) used 58 days of CuPIDO station observations around and over the CM to show that the katabatic, nocturnal, and anabatic daytime surface flows tend to be in phase with the horizontal perturbation pressure gradient force (PGF), which tends to be directed away from and toward the CM during the night and day, respectively. Clearly a horizontal hydrostatic PGF cannot be computed between stations at vastly different elevations without an assumption about the temperature profile between the station elevations. Geerts et al. (2008) first remove the 24-h mean pressure at each station, and then examine the diurnal variation of the perturbation pressure *difference* between the ISFF stations and Mt. Bigelow (Fig. 2), after accounting for the effect of the diurnal temperature cycle at the valley and mountain stations. This technique is used in Fig. 5d for the 12 July case. The observed “anabatic forcing” period (when the perturbation pressure difference is positive, i.e., lower pressure over the mountain) lagged the 10-point surface MSC by a few hours. This apparent lag will be revisited below (section 4). The modeled horizontal perturbation pressure difference (Fig. 5e) matches the observed trend very well, even in the comparison for individual stations, suggesting that the WRF simulation captures the diurnal evolution of the lower-tropospheric temperature variation over the CM.

## 2) WRF SURFACE CONDITIONS

The predawn (1200 UTC) surface map for 12 July shows flow around the CM obstacle and strong drainage flow (Fig. 6). The ambient northwest wind blows at higher elevations of the CM. The convergent flow on the lee (southeast) side produces a deeper PBL there in the early morning hours (east–west transects above the maps in Fig. 6). Nocturnal cooling is more intense in the Tucson valley than in the San Pedro valley (unlike most other CuPIDO days), and the San Pedro valley remains 1–2 K warmer than the Tucson valley during the day (Fig. 6), consistent with observations (Fig. 5a). This east–west baroclinicity in the CBL is also observed and WRF simulated on several other CuPIDO days before 25 July 2006, the start of the wet monsoon (Damiani et al. 2008). The reason appears to be a higher sensible heat flux due to the lower soil moisture in the San Pedro valley.

By 1600 UTC, northerly flow develops over most of the WRF inner domain with a clear upslope wind component over the higher elevations (but below  $\sim 2000$  m MSL), especially through Canyon del Oro. A cyclonic eddy develops just southwest of the CM between 1600 and 1800 UTC (confirmed by a few ISFF wind barbs, Fig. 6) with anabatic flow into Bear Canyon. By 1800 UTC (Fig. 6), north-northeast flow envelops the domain, stronger and more uniform than observations suggest. The CBL top over the valley reaches mountain top level at about 2000 UTC, resulting in a rather uniform potential temperature distribution. The CBL continues to deepen throughout the afternoon, reaching a maximum depth of  $\sim 3$  km over the domain by 2300 UTC (Fig. 4). The deep PBL results in a more uniform NW surface wind field, with little evidence of the terrain-as-an-obstacle effect. There is still some evidence of upslope flow but it may be mechanically rather than thermally forced. Because the model surface temperatures are  $\sim 2$  K warmer than observed, the PBL depth is probably exaggerated across the domain.

We compute MSC of surface (10 m) flow at 1-km resolution using square boxes centered on Mt. Lemmon, with lengths of 10, 20, 30, and 40 km (Fig. 2). It appears that in this case a line integral over 10 points (collocated with ISFF stations with an average separation of 10 km) is insufficient to capture the surface MSC (Fig. 5c), since more persistent and stronger daytime MSC is computed using a 1-km resolution for the 400 and 900 km<sup>2</sup> boxes, with surface areas most closely matching the ISFF polygon area (Fig. 7). The trend of MSC at these scales corresponds better with the WRF anabatic forcing period (Fig. 5e). The steepness of the CM terrain at a resolution of 1 km can lead to spurious pressure gradients even with terrain-following coordinates (Klemp et al. 2003) and

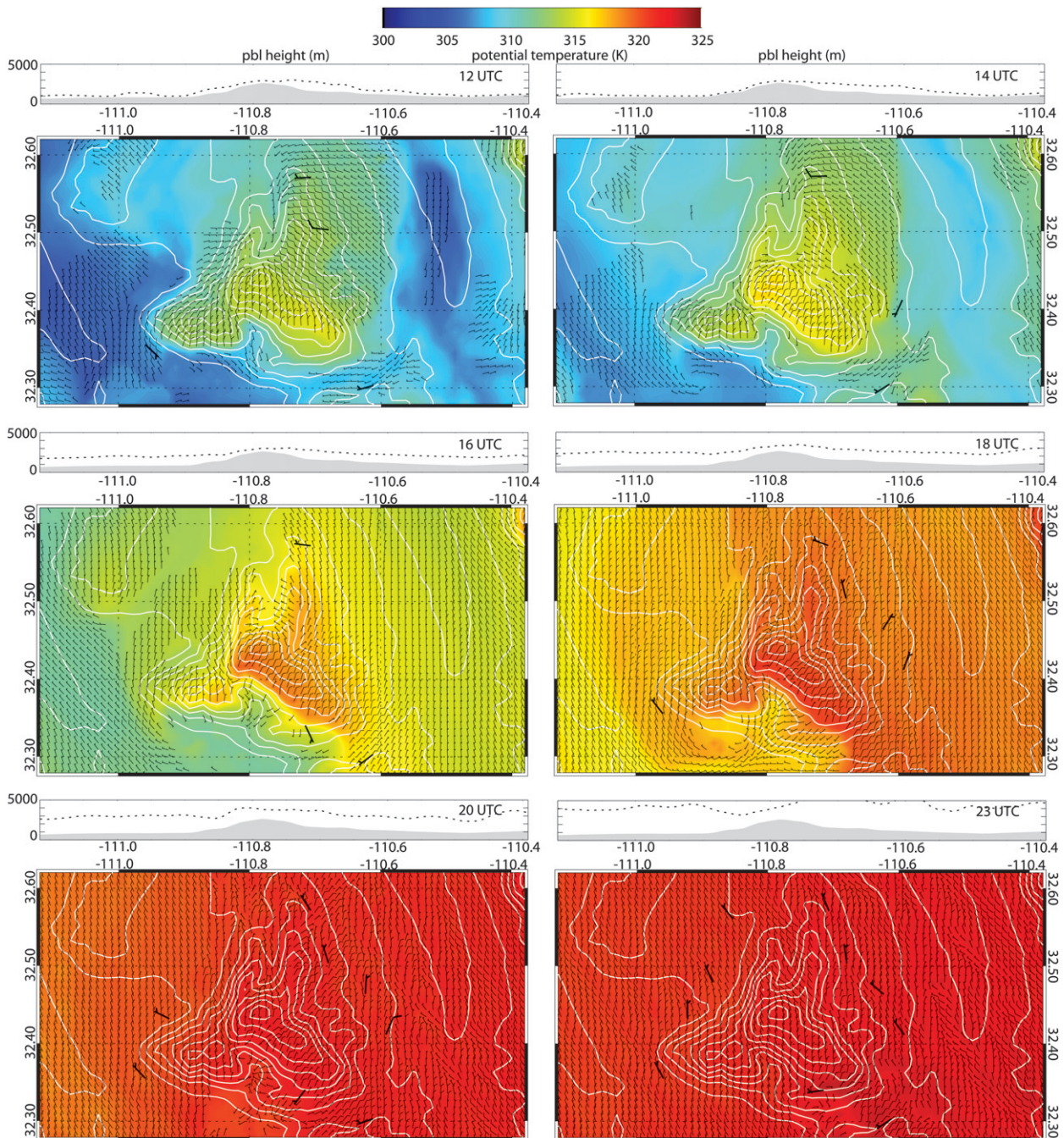


FIG. 6. Inner-domain maps of 2-m potential temperature (color) and 10-m winds (thin bars) with terrain contours (white) for 1200, 1400, 1600, 1800, 2000, and 2300 UTC 12 Jul 2006. Observed ISFF 30-min average winds for corresponding times are also shown, with bold wind bars. Above each map is an east–west PBL height (dashed line) and terrain (gray shading) cross section across Mt. Lemmon between 0 and 5000 m above mean sea level.

thus unreasonable velocities. WRF version 3.0 does remarkably well. The trend of surface MSC is rather symmetric for the four boxes over Mt. Lemmon, suggesting no interruption by moist convection.

The inverse relationship between box size and MSC (i.e., the smaller the box, the larger both nighttime divergence

and daytime convergence) makes intuitive sense, as the slope is steepest along the perimeter of the smallest box and area decreases. The period of daytime surface MSC decreases with decreasing box size. This would make sense if the CBL over the surrounding valleys was rather shallow compared to the mountain, and only briefly grew

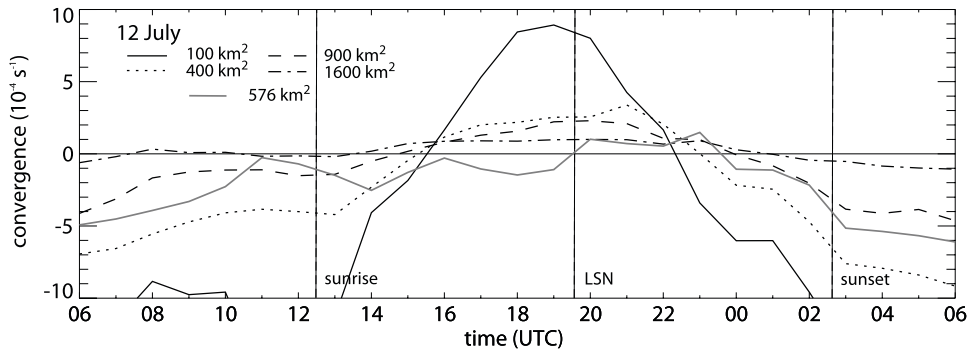


FIG. 7. WRF-based surface MSC for 100, 400, 900, and 1600 km<sup>2</sup> square boxes and for the 10 grid points closest to the ISFF stations (a 576 km<sup>2</sup> polygon), for the 12 Jul 2006 case. Also shown is the 10-station observed MSC.

deeper than the mountain top. But that is not the case (Fig. 4). It occurs on other simulated CuPIDO days as well, although less pronounced, and it is most apparent in the early cessation of MSC in the afternoon in the smaller box. The likely explanation is found in the surface energy budget. The early onset of divergent flow in the afternoon along the perimeter of the smallest box (i.e., along the steeper terrain close to Mt. Lemmon), as early as 4 h before sunset, is consistent with the early change in sign of the average surface net radiation within that box. In the two largest boxes composed of less steep terrain, surface divergence only commences 1 h before sunset, and the change in sign of the mean surface net radiation is also delayed. This will be explored further in a separate study focusing on the surface energy budget and MSC.

### 3) VERTICAL STRUCTURE

We found the afternoon surface flow around the mountain to be convergent both in the data (Fig. 5c) and in the model on 12 July (Fig. 7). Is this anabatic flow part of a closed cell (toroidal ring around the mountain) with divergent return flow aloft, as is conceptually understood [e.g., Fig. 1 in Demko et al. (2009)]? And if so, is this circulation solenoidally forced (i.e., is there a warm anomaly over the mountain within a well-mixed CBL)? Both the return flow aloft and a warm anomaly over the CM are very difficult to detect in the CuPIDO data (Demko et al. 2009). Aircraft data from two CM circumnavigations, at 300 m AGL and 780 hPa (below mountain top), show a distinct positive virtual potential temperature anomaly ( $\theta'_v$ ) of about 1 K close to the mountain slope on just 1 of 3 days (Demko et al. 2009). The most solid measure of the solenoidal forcing is the daytime negative hydrostatic pressure perturbation over the CM on 12 July (Fig. 5d) and on most days during CuPIDO (Geerts et al. 2008). We now use WRF output

to examine both the solenoidal return flow and the solenoidal forcing.

The flow and temperature variations are dominated by convective eddies in the CBL. To reveal the mean solenoidal flow and its forcing, some averaging is needed. To retain the temporal dimension (so we can examine evolution), we decided to average spatially. The CM and surrounding valleys stretch from the north-northwest to the south-southeast (Fig. 1). Therefore, it makes sense to average along the main axis, rather than over a series of azimuths. An average of 21 west–east (actually, west-southwest to east-southeast) slices, composing 21 km along the CM's main axis, is shown in Fig. 8. The afternoon surface west–east baroclinicity mentioned above occupies much of the depth of the CBL, as is evident in the mean profile on Fig. 8d. Such baroclinicity certainly has dynamical implications, including a deeper CBL on the east side and a tendency for westerly sea-breeze-like flow to occur on the southern and northern edges of the CM. But in order to better tease out the solenoidal forcing, we examine potential temperature departures ( $\theta'_{we}$ ) from the mean value either to the east ( $\overline{\theta'_{east}}$ ) or the west ( $\overline{\theta'_{west}}$ ) of the CM crest, at any level. And in order to detect a solenoidal circulation, we examine the zonal wind perturbation ( $u'$ ), that is, the departure from the mean wind ( $\bar{u}$ , computed across the full transect) at any level. The profiles of the mean potential temperature ( $\overline{\theta'_{east}}$  and  $\overline{\theta'_{west}}$ ) and  $\bar{u}$  are shown in Fig. 8. Clearly the mean wind can influence the potential temperature and vertical velocity pattern above the PBL (e.g., a westerly flow above the CBL can produce subsidence and a warm anomaly in the lee of the crest). But the mean zonal wind is weak and the CBL deep (Fig. 8). The emphasis of this analysis is on the thermally forced circulation.

Before dawn the low-level ambient northwesterly flow produces subsidence as strong as  $5 \text{ m s}^{-1}$  just east of the mountain crest (Fig. 8). This subsident flow is not felt farther down at the ISFF stations. This downslope

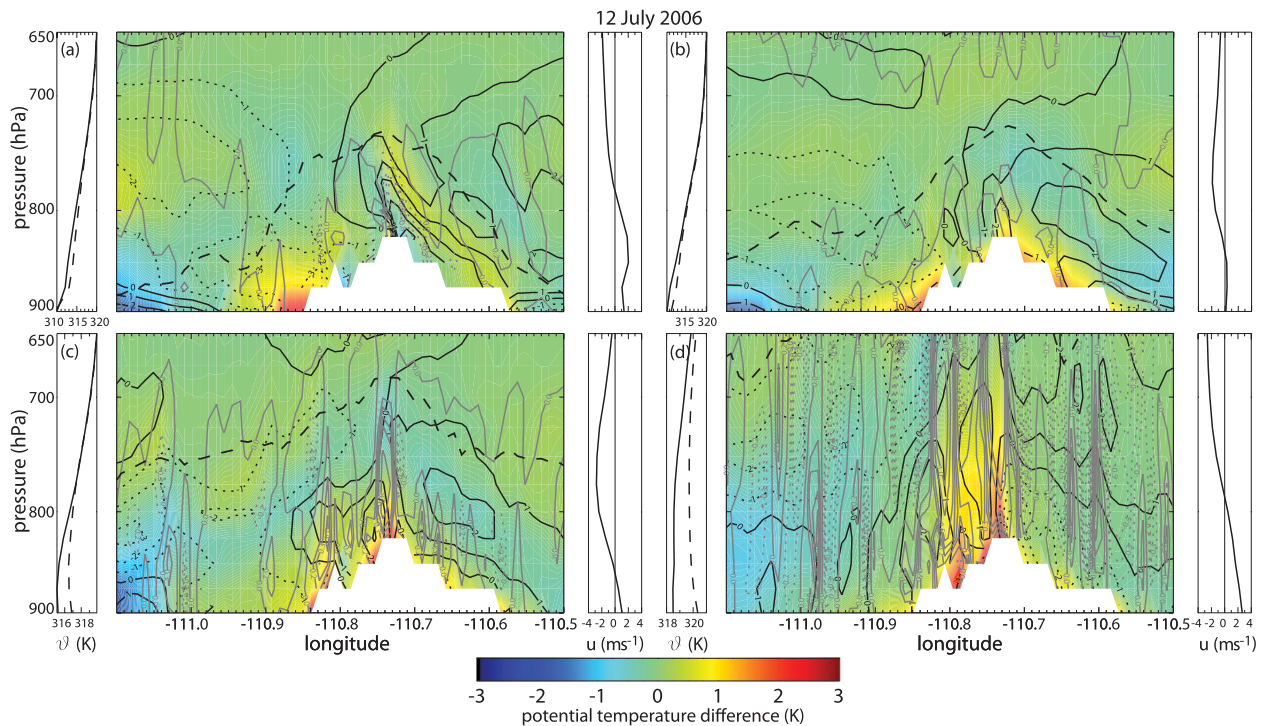


FIG. 8. East–west cross section based on an average of 21 points (21 km) in the north–south direction (i.e., along the main axis of the CM) for (a) 1200, (b) 1500, (c) 1800, and (d) 2100 UTC 12 Jul 2006. The white area is the 21-km-averaged terrain height. The cross section shows  $\theta'_{we}$  (color fill),  $u'$  (solid black contours for westerly flow and dotted black contours for easterly flow, contour interval  $1 \text{ m s}^{-1}$ ),  $w$  (solid gray contours for updrafts and dotted gray contours for downdrafts, contour interval  $0.2 \text{ m s}^{-1}$ ), and PBL height (long-dashed black line). Also shown are profiles of  $\bar{\theta}'_{west}$  (solid) and  $\bar{\theta}'_{east}$  (dashed) on the left of each cross section, and  $\bar{u}$  on the right. The variables are defined in the text.

flow weakens as the PBL deepens, and by 1800 UTC shallow upslope flow is present on the east side. Deeper upslope flow is present on the west side, with some easterly return flow above, indicating divergent flow near the PBL top. At this time the ambient flow between 850 and 700 hPa is essentially northerly (out of the page). A shallow warm anomaly ( $\theta'_{we} > 0$ ) is present over the mountain slopes by 1500 UTC, but updrafts in the PBL still are weak and shallow. By 1800 UTC, an updraft peaking at  $0.9 \text{ m s}^{-1}$  is found over the highest terrain. This updraft is contained within the CBL and decays where the zonal flow is divergent, clearly indicating a solenoidal circulation contained within the CBL on the mountain's west side. This updraft is buoyant at its base and slightly cooler than the ambient air near its top, suggesting slight overshooting and CBL growth. Clearly the solenoidal inflow advects cooler air, yet both the warm anomaly and the solenoidal flow are still there, even stronger, at 2100 UTC (1.5 h after solar noon), so the cold air advection must be entirely offset by sensible heat flux convergence in the CBL over the elevated terrain. Surface heating must cause this warm anomaly as it is strongest near the surface.

The CBL has deepened to 550 hPa over the CM by 2100 UTC, well above the upper boundary in Fig. 8d. The warm dome over the mountain is approximately 15 km wide, extends over the lower half of the CBL, and has a strength of up to 3 K. The anabatic flow is rather symmetric on both sides with maxima in  $u'$  located well above the surface. Remarkably symmetric diffluent flow exists aloft. This return flow is mostly contained within the CBL (not shown). Deep updrafts approaching  $1.5 \text{ m s}^{-1}$  prevail over the CM high ridge and over the lower ridge on the west side, with sinking motion prevailing over the surrounding valleys. Thus, Fig. 8d nicely illustrates a rather symmetric thermally direct circulation and its solenoidal forcing over the mountain.

The model output can be used to calculate MSC within any given area at all pressure levels, and to construct a time–height diagram of MSC (Fig. 9). We use the  $30 \times 30 \text{ km}^2$  box because it encompasses the majority of the CM footprint and generally does not intersect high terrain (Fig. 2). Note that the *surface* MSC (based on 10-m winds) is not computed at a constant pressure level, but rather along the undulating terrain along the box perimeter. In Fig. 9, the surface MSC is assigned an

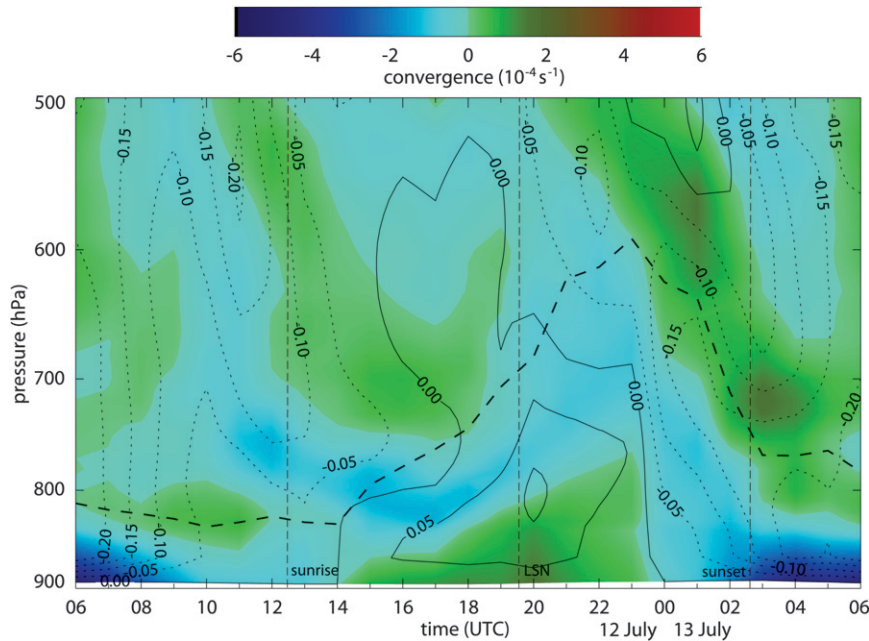


FIG. 9. Time–height plot of MSC for the 900 km<sup>2</sup> box (color shaded), mountain-scale vertical velocity within this box inferred from mass continuity (solid lines for updrafts, dotted lines for downdrafts, contour interval 0.05 m s<sup>-1</sup>), and mean PBL height along the box perimeter (bold dashed line), for the 12 Jul 2006 case.

altitude corresponding with the average pressure along this perimeter. Constant-pressure MSC values are only available above the highest elevation along the box perimeter, a level considerably above the mean altitude of the surface MSC. For instance, for the 30 × 30 km<sup>2</sup> box, the average pressure for the surface MSC is 895 hPa and the lowest level of constant-pressure MSC values is 840 hPa. The mountain-scale vertical velocity  $w_{MS}$  then is computed from the MSC profile from air mass continuity:

$$w_{MS}(p) = \frac{\rho(p_0)}{\rho(p)} w_{MS,0} - \frac{1}{g\rho(p)} \int_{p_0}^p \text{MSC}(p) dp, \quad (1)$$

where  $\rho$  is air density,  $g$  gravity, and the vertical increment  $\Delta p$  is 55 hPa in the lowest layer and 10 hPa above 840 hPa. We assume  $w_{MS,0} = 0$ . This assumption is reasonable, since  $w_{MS}(p)$  is almost identical to the average vertical velocity within the 30 × 30 km<sup>2</sup> box at any pressure level. The profiles of MSC and  $w_{MS}$  on 12 July are shown in Fig. 9. The lack of vertical resolution between 895 ( $p_0$ ) and 840 hPa should be noted, thus nocturnal drainage flow is not captured well, and its depth is exaggerated. The surface flow becomes convergent about 2 h after sunrise and at the same time divergent flow establishes near the PBL top. This convergent flow gradually deepens during the day; in fact between 1500 and 2300 UTC the level of nondivergence

within the CBL rises at the same rate as the CBL height. Most of the upper-level divergence remains contained within the CBL. Even though there is no capping stable layer in the model sounding over the mountain at any time between 1500 and 2300 UTC, the upper-level divergence generally compensates the low-level convergence and there is little mountain-scale vertical motion above the CBL. The lack of mass flux above the CBL is consistent with the absence of orographic cumulus convection on 12 July (Fig. 4). Within the CBL  $w_{MS}$  peaked at 0.12 m s<sup>-1</sup> at a scale of 30 × 30 km<sup>2</sup>. After 0000 UTC, the MSC profile becomes divergent near the surface while the flow in the residual mixed layer becomes convergent. This elevated MSC, which appears to descend with time, does not produce any cumulus convection on this day, both in the model and in reality.

#### 4) FORCING OF THE ANABATIC SURFACE FLOW

We now revisit the forcing of the anabatic surface flow. While in Fig. 5e the perturbation horizontal perturbation pressure difference is computed between Mt. Lemmon and the grid points nearest the ISFF stations, in Fig. 10 it is computed between Mt. Lemmon and the average for all grid points on the perimeter of boxes of various sizes centered on Mt. Lemmon (Fig. 2). Also shown in Fig. 10 is the time series of surface MSC for the respective boxes, allowing for a direct comparison of

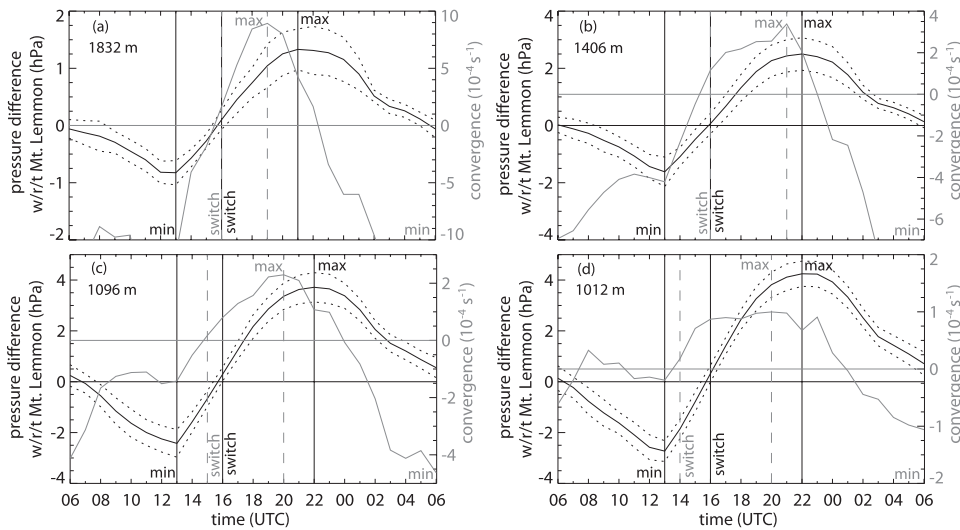


FIG. 10. Time series of the mean perturbation horizontal pressure difference between points along a square box and Mt. Lemmon (black solid line, left axis) and MSC for the corresponding box (gray lines, right axis) for (a) 100, (b) 400, (c) 900, and (d) 1600 km<sup>2</sup> boxes, for the 12 Jul 2006 case. The black dotted lines indicate the mean pressure difference  $\pm 1\sigma$ , based on all grid points of the box's perimeter. A positive pressure difference implies a lower perturbation pressure at Mt. Lemmon (i.e., anabatic "forcing"). Black solid vertical lines highlight the time that the pressure difference is minimum, switches sign, and is maximum, respectively. Gray dashed vertical lines highlight the same for MSC. The average height MSL of points along each box perimeter is shown in the top-left side of each panel. For comparison, the elevation of Mt. Lemmon in the inner WRF domain is 2629 m MSL.

Fig. 10 with the 2-month composite in Geerts et al. (2008, their Fig. 5).

The anabatic forcing period is rather scale independent on 12 July, unlike the period of surface MSC. It slightly lags behind the movement of the sun and thus the surface sensible heat flux: the katabatic forcing is largest near sunrise and anabatic forcing commences 2.5 h after sunrise, to peak 2–3 h after solar noon, for all boxes. This makes sense because the growth of the CBL is delayed relative to surface heating (e.g., Fig. 9). Yet it is less intuitive why the anabatic forcing lags behind the surface MSC: there is a 0–2-h lag of the start of anabatic forcing relative to the start of anabatic flow, and the peak anabatic forcing lags 1–2 h behind the peak anabatic flow, depending on the size of the box (Fig. 10).

A flow should respond to a pressure gradient forcing, so it is hard to conceive that it leads rather than lags. The counterintuitive lag in anabatic forcing is also seen in the composite surface observations over the CM [see Fig. 5 in Geerts et al. (2008)]. The lag in anabatic forcing relative to the surface MSC is most apparent in the late afternoon. The perturbation pressure difference only becomes negative a few hours after sunset, yet the surface flow becomes divergent several hours before sunset. This is the key to solve the apparent inconsistency. While the flow in the thin radiatively cooled layer near the surface becomes katabatic before sunset, the pressure

gradient force (which operates over a greater depth) remains anabatic until well after sunset, producing elevated MSC decoupled from the surface. This decoupling from the friction layer may explain the rather strong MSC above the surface just after sunset (Fig. 9). Similarly, the surface flow hugging the heated terrain may become upslope in the morning before the warm anomaly over the mountain is deep enough to result in anabatic forcing.

#### b. 9 July 2006: A case with simulated orographic *Cu mediocris* producing a trace of rain

##### 1) MODEL VALIDATION

The day of 9 July 2006 started out with a deep potentially unstable layer above a shallow stable layer in the Tucson valley (Fig. 11). Both model and observed soundings reveal a deep residual mixed layer between 875 and 600 hPa. The most notable difference between observed and model sounding resides in the moisture profile: the WRF profile contains 2–3 g kg<sup>-1</sup> less water vapor below 600 hPa compared to observations. The difference in low-level moisture is important: the observed sounding has a most-unstable CAPE of 1170 J kg<sup>-1</sup> and an equilibrium level just above the 200-hPa level (Fig. 11b). The WRF sounding has less CAPE (155 J kg<sup>-1</sup>), yet it has substantial potential instability between 850 and

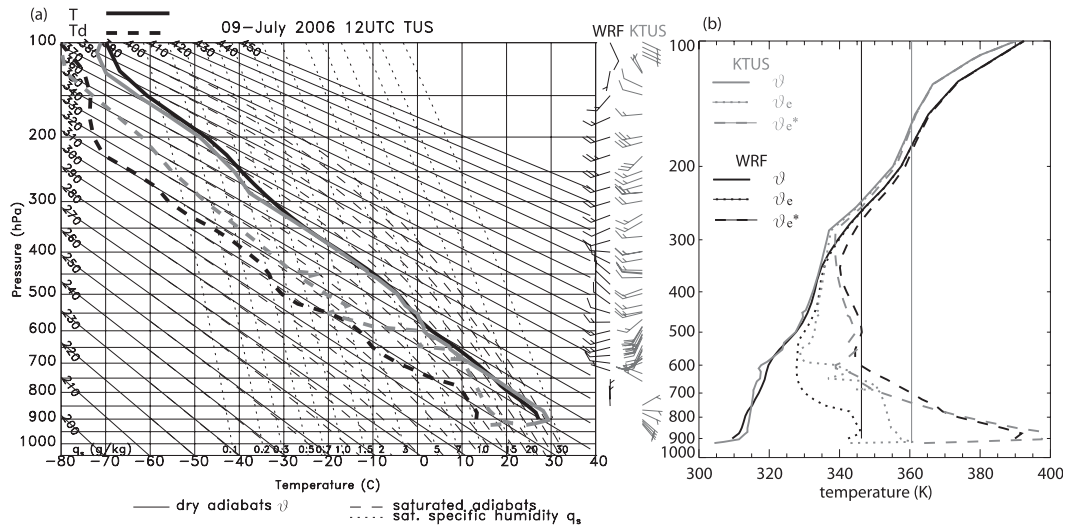


FIG. 11. As in Fig. 3, but for 1200 UTC 9 Jul 2006.

650 hPa. WRF captures the wind profile well: weak and variable wind below the mountain top and southwest winds ranging between 4 and 14 m s<sup>-1</sup> above the mountain top. Compared to the 12 July case (Fig. 3), the 9 July case had more CAPE, higher low-level humidity, a lower surface temperature, and a lower LCL. The wind profiles in the two cases were quite similar.

Deep convection did not develop on 9 July: during the morning hours the mixing ratio at the ISFF stations decreased from ~12 to 8 g kg<sup>-1</sup>, likely decreasing the CAPE from its 1200 UTC value at KTUS. (No CuPIDO soundings were collected on this day, so it cannot be confirmed.) Altostratus partly covered the sky for ~2 h after sunrise, and shallow cumuli developed over the CM, from 3.6 h before solar noon into the early afternoon, with a maximum cloud top of 4.4 km at solar noon (Fig. 12), and a maximum cloud depth of ~1.5 km. The orographic Cu drifted to the east with the prevailing westerly flow aloft (Fig. 12b).

The drying trend in the model is smaller, and the observed humidity at ISFS stations matches that at corresponding grid points well. By 1700 UTC, the CAPE over the mountain has increased to 400 J kg<sup>-1</sup> and CIN has decreased to 60 J kg<sup>-1</sup> (Fig. 12a). Orographic Cu are present in the WRF simulation during roughly the same period as observed, but they grow deeper, with a maximum cloud top of 5.5 km (just above the freezing level) and a maximum cloud depth of 2.8 km at 1900 UTC. The model cloud-top data in Fig. 12 are based on the highest grid point in a 30 × 30 km<sup>2</sup> box around Mt. Lemmon with at least 0.01 g m<sup>-3</sup> cloud liquid water and ice in the WRF output. Model Cu tend to form over the highest terrain and drift to the east, as observed. The maximum cloud depth is sufficient for WRF to produce a trace of precipitation.

Stations east of Mt. Lemmon recorded a higher potential temperature at night, compared to those on the west side, since they are generally at a higher elevation

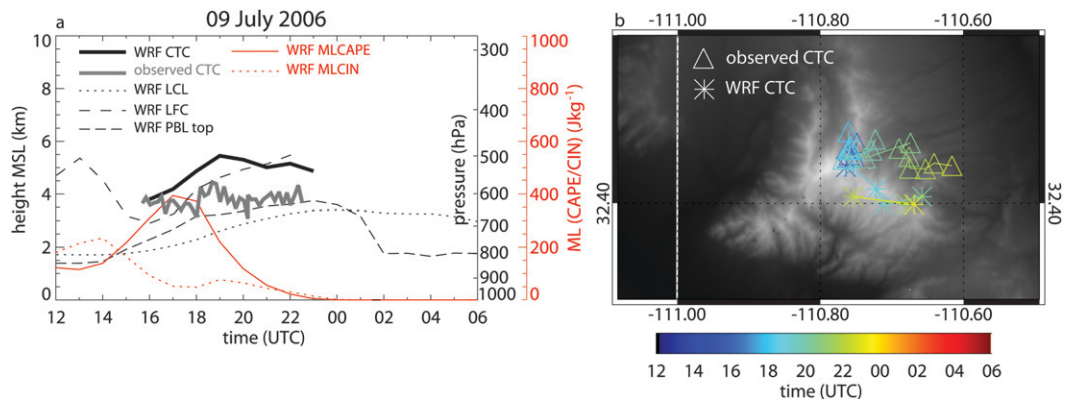


FIG. 12. As in Fig. 4, but for the 9 Jul 2006 case.

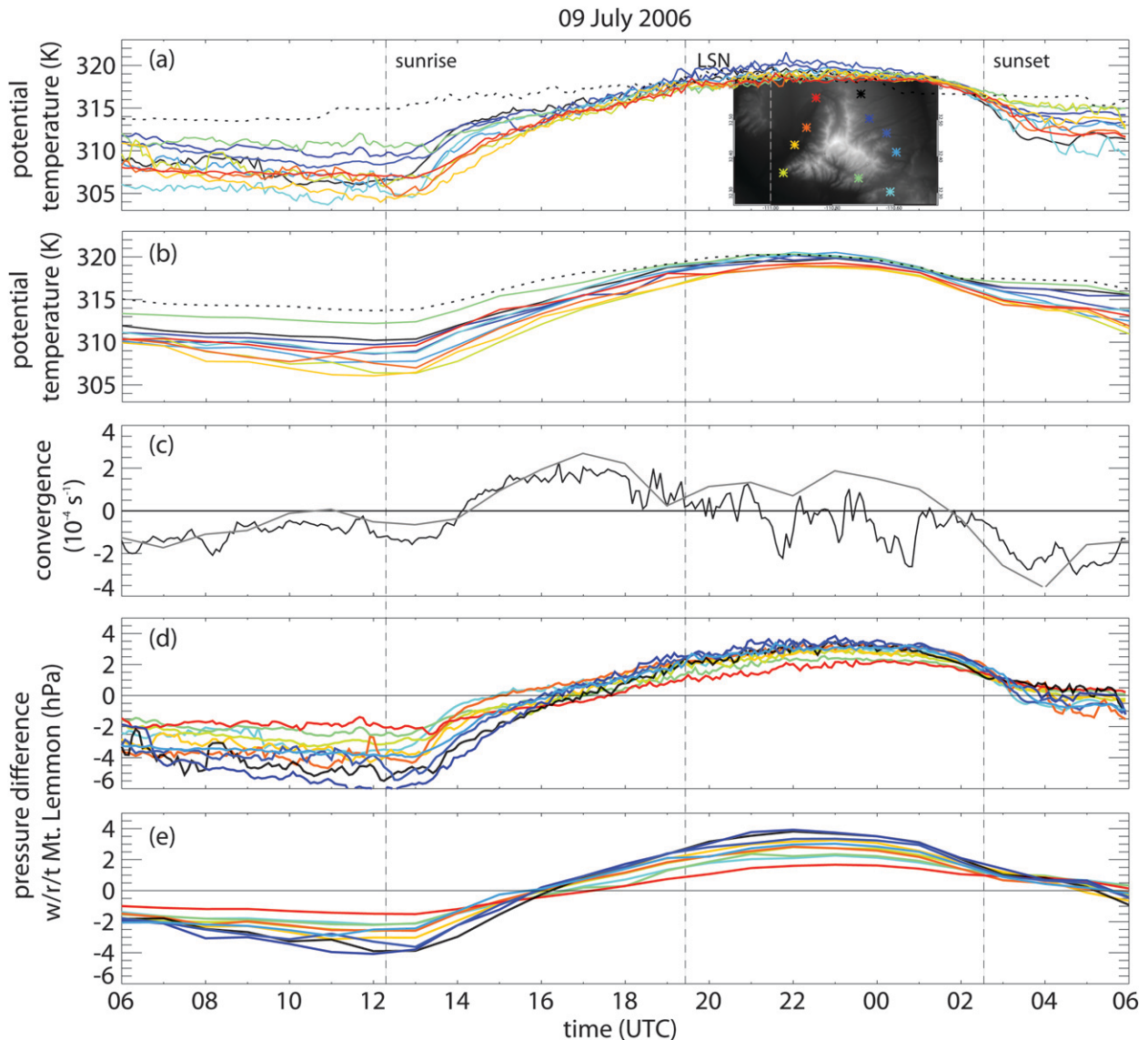


FIG. 13. As in Fig. 5, but for the 9 Jul 2006 case.

or on local ridges there (Fig. 13a). The model underestimates nocturnal cooling by  $\sim 2$  K at most stations. The east side remained slightly warmer than the west side as the CBL developed, as in the 12 July case. Again WRF nicely captures this east–west baroclinicity, 1–2 K in magnitude (Fig. 13b).

WRF also captures the magnitude and diurnal variation of the surface MSC quite well (Fig. 13c). The observed surface flow was divergent at night and in the early morning. The MSC developed  $\sim 1.5$  h after sunrise, peaked  $\sim 1.5$  h before solar noon, and terminated remarkably early ( $\sim 2100$  UTC), which is replicated quite well by WRF. On 12 July (Fig. 5c) and on other CuPIDO days without lightning, MSC generally persisted at least

until 0000 UTC [see Fig. 8 in Geerts et al. (2008)]. On 9 July the MSC may have become negative rather early because westerly momentum was carried down on the lee of the CM in a deep CBL. (There was a weak westerly jet at  $\sim 650$  hPa in the 0000 UTC 10 July KTUS sounding.) Orographic Cu remained present until 2230 UTC (Fig. 12a), thus for some time they were not supported by surface MSC. The modeled flow remains convergent until evening, and is more convergent for this day than for 12 July.

Observed (Fig. 13d) and modeled (Fig. 13e) perturbation pressure differences compare quite well, as on 12 July, and again they lag the MSC by a few hours, especially in the evening.

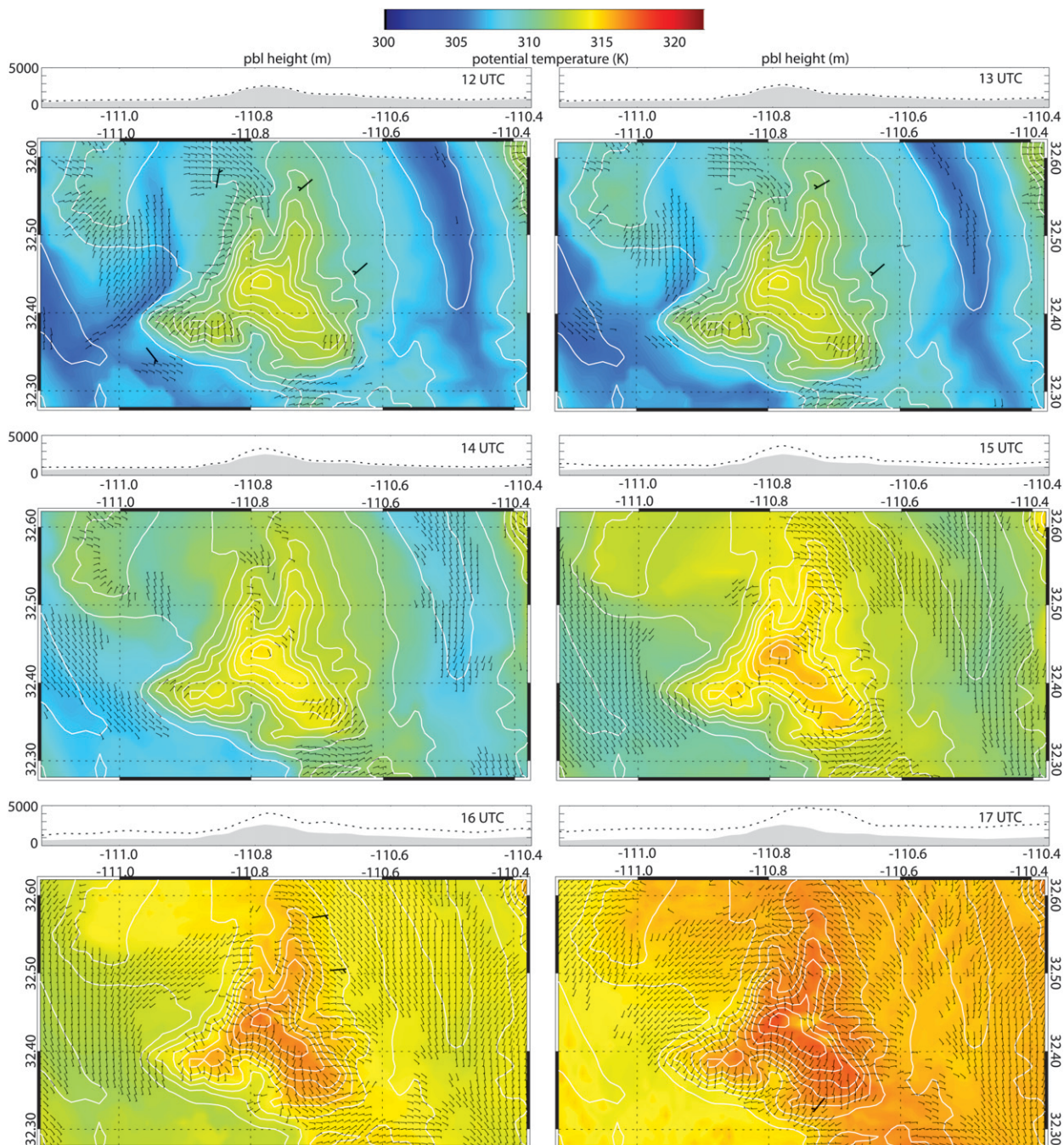


FIG. 14. As in Fig. 6, but hourly between 1200 and 1700 UTC for the 9 Jul 2006 case.

2) WRF SURFACE CONDITIONS

Drainage flows can be seen especially in lower valleys and mountain canyons from 1200 to 1400 UTC (Fig. 14). By 1500 UTC, drainage flow is still present in lower valleys; however, winds become convergent near the CM as the PBL deepens, consistent with basic theory (e.g., Whiteman 2000). The flow becomes mainly southeasterly

by 1600 UTC (Fig. 14) on both sides of the CM in lower elevations, with clearly confluent flow toward the higher elevations, specifically toward Pusch and Bigelow ridges (Fig. 2). The anabatic flow tends to channel in canyons, such as Bear Canyon. Throughout the morning hours, the observed winds were too weak to be plotted (i.e., <5 kt; Fig. 14). In the afternoon the WRF surface winds correspond reasonably with the observed winds. The San Pedro

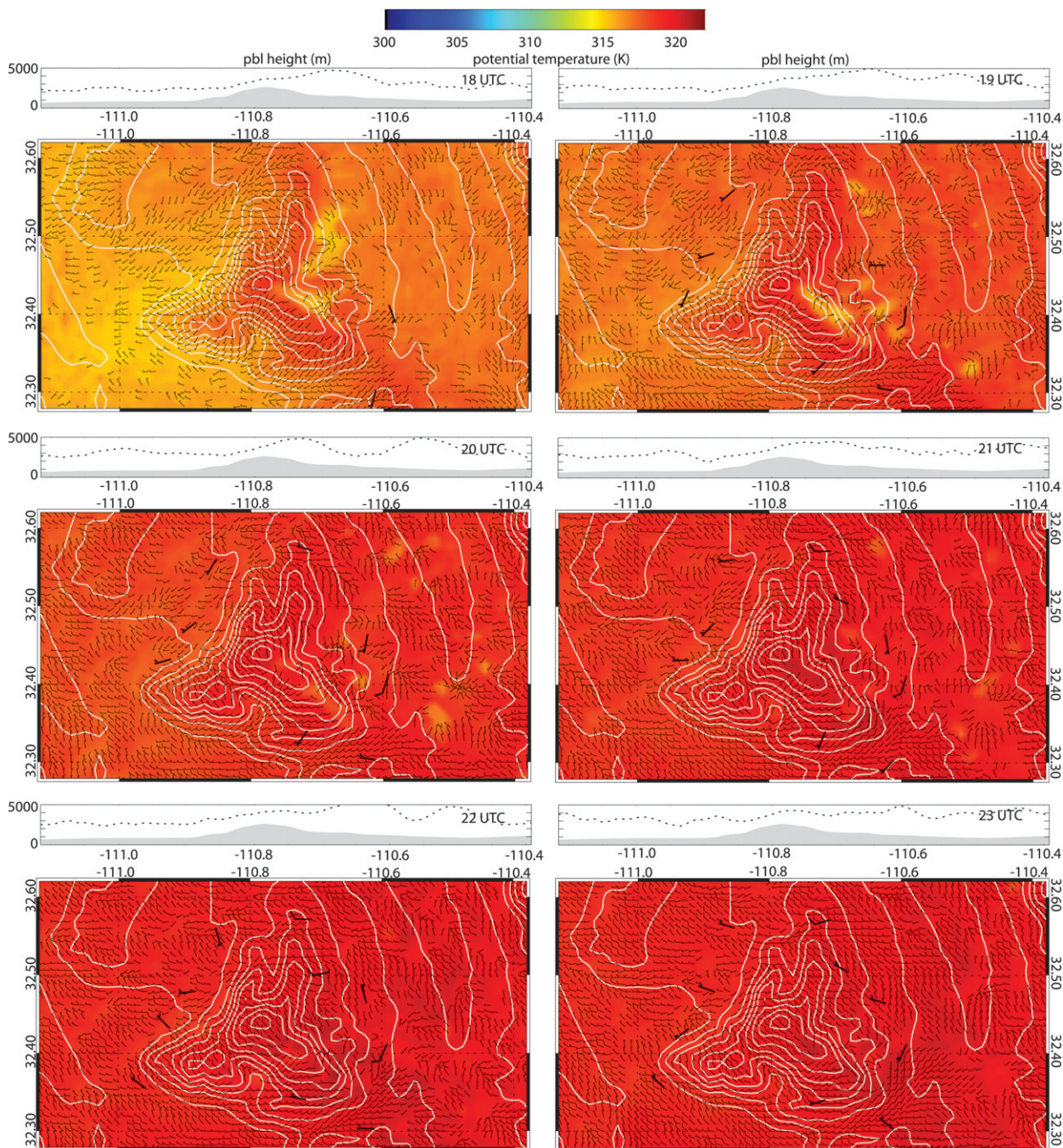


FIG. 15. As in Fig. 14, but for 1800–2300 UTC.

Valley is generally warmer than the Tucson Valley during the CBL growth period, mainly between 1500 and 1900 UTC, as on 9 July; therefore, the CBL grows deeper over the San Pedro Valley.

Several small cold pools can be seen during 1800–2000 UTC over Bigelow Ridge and on the east side, downwind from the CM (Fig. 15); the surface flow is clearly divergent around these pools at 1900 UTC. These

cold pools are attributed to resolved moist convection (Fig. 12), which we mapped in 3D using Integrated Data Viewer (IDV) software (not shown). The typical diameter of the cold pools is 5 km, and the associated cumulus convection is only marginally resolved in the inner domain, with a grid spacing of 1 km. A trace of precipitation fell in the cold pools between 1800 and 2000 UTC. Model sensitivity tests were conducted to

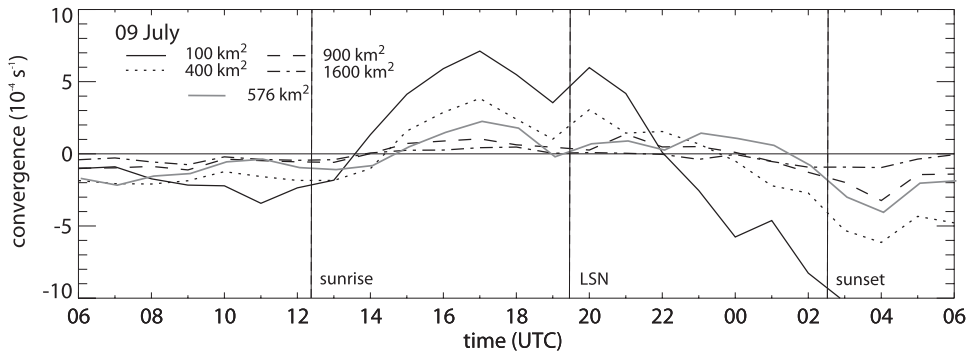


FIG. 16. As in Fig. 7, but for the 9 Jul 2006 case.

examine whether these cold pools are due to cloud shading or to convective downdraft processes (i.e., evaporation of rain below cloud base and downward transport of lower  $\theta_e$ ). Turning off the option “cloud shading” (i.e., the effect of clouds on the surface energy balance) weakens but does not destroy the cold pools. The no-cloud-shading simulation actually produces stronger MSC, deeper convection, and up to 4 mm of rain at 1900–2000 UTC (not shown), indicating that orographic cloudiness acts as a negative feedback to orographic convection by suppressing the surface net radiation and sensible heat flux. Only a dry simulation (no cloud microphysics, no latent heat exchange) entirely removes the cold pools. Nonprecipitating Cu clouds are still present between 2100 and 2300 UTC in the default simulation (Fig. 12), but their surface footprint is weaker (Fig. 15). Thus, both cloud shading and convective downdraft processes contribute to the cold pools.

Remarkably, the divergent flow near Bigelow Ridge at 1900 UTC (Fig. 15), induced by a convective towers less than 3 km deep producing just a trace of precipitation, is sufficient to temporarily change the sign of the integrated MSC (Fig. 13c). Closer examination shows an immediate response (at 1900 UTC) in the 100 and 400 km<sup>2</sup> boxes, a delayed response (at 2000 UTC) in the 900 km<sup>2</sup> box, and no response in the 1600 km<sup>2</sup> box (Fig. 16). The effect of cold-pool spreading on MSC and successive convective development is explored further in Part II.

### 3) VERTICAL STRUCTURE

The mean flow in a cross section of average conditions along the main axis of the CM is insignificant, except for a westerly jet near 650 hPa before noon (Fig. 17). Aside from the minor effect of this jet on the temperature and wind field above the PBL, the evolution displayed in Fig. 17 is clearly due to surface heating. There is evidence of a shallow stable layer and drainage flow before sunrise at 1200 UTC, especially in the San Pedro Valley.

By 1500 UTC (Fig. 17b), the PBL depth has increased more over the CM than over the surrounding plains, and a shallow warm anomaly ( $\theta'_{we} > 0$ ) hugs the mountain slopes. The near-surface flow has become convergent (Fig. 16), with  $u' > 0$  on the western slopes and, less evidently,  $u' < 0$  on the eastern slopes. The developing anabatic flow contributes to weak ascent especially along the western slopes. The slivers of updrafts evident at times when the CBL is well developed (Figs. 17c,d) are primarily due to buoyant CBL thermals, whose dominant scale is near the resolution limit of this model simulation, and much smaller than that of the CM.

The CBL has become quite deep by 1800 UTC (Fig. 17c), up to about 630 hPa over the CM, and deeper over the San Pedro Valley than over the Tucson Valley. The shallow anabatic flow is well established at up to 3 m s<sup>-1</sup> on the western slopes and 2 m s<sup>-1</sup> over the eastern slopes. Divergence in the upper PBL is apparent as well, with easterly (westerly) outflow at 1–2 m s<sup>-1</sup> on the western (eastern) side of the CM, but the center of divergence is tilted toward the east of the mountain because of the prevailing westerly flow. The warm anomaly over the CM continues to be shallow. Its effect on hydrostatic pressure reduction over the mountain is partially offset by a cold anomaly in the upper PBL. Thus, at 1800 UTC the horizontal perturbation pressure difference between the mountain and the surrounding foothills is very small (Fig. 13e), smaller than at 2100 UTC when the warm anomaly over the mountain is deeper.

The weak mean westerly flow from the surface to 650 hPa at 2100 UTC (Fig. 17d) is due to vertical mixing of westerly momentum from aloft. This flow shifts the convergence and associated slices of strong ascent toward the leeside (eastern) foothills, consistent with observations and simulations over other mountain ranges (Banta 1984; Tucker and Crook 2005). Thus, it is over the eastern foothills, where the PBL is deepest, that shallow cumulus convection occurs, both in reality and

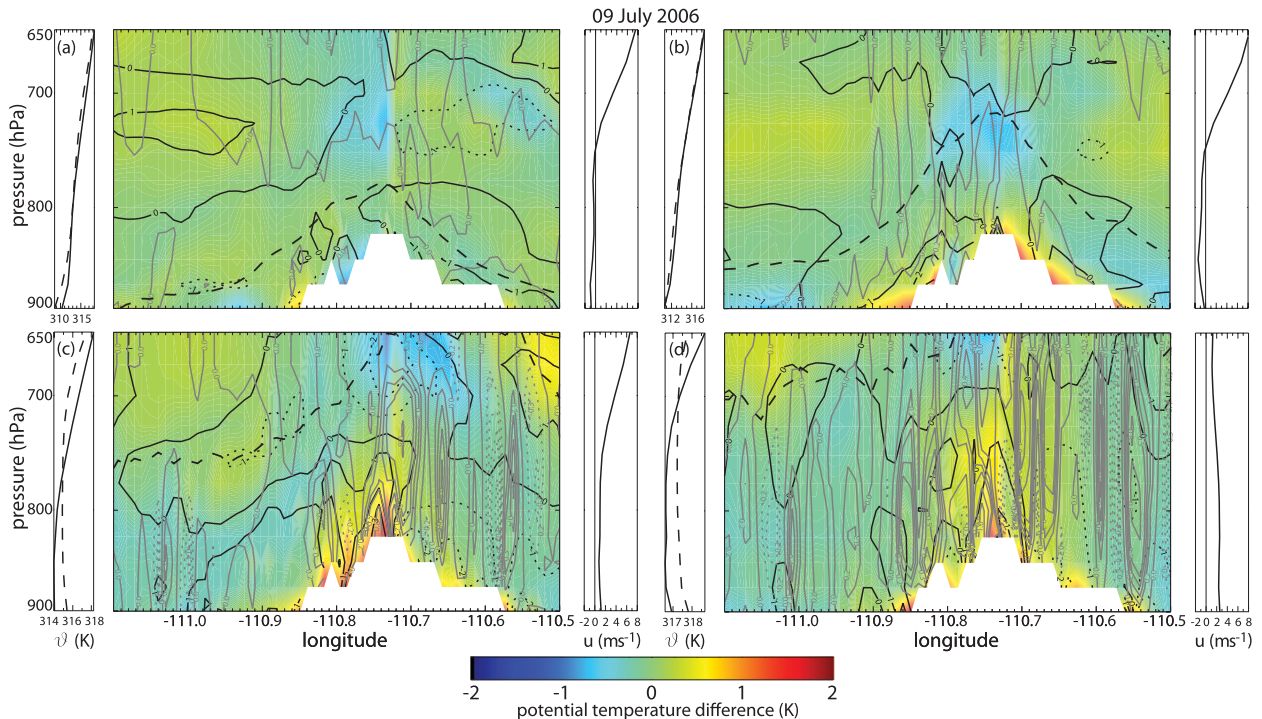


FIG. 17. As in Fig. 8, but for the 9 Jul 2006 case.

in the model (Figs. 12 and 15). The MSC has weakened at the surface by 2100 UTC (Fig. 16), yet it has deepened, almost encompassing the entire CBL, with divergence occurring at or above the CBL top near 600 hPa (Fig. 17d).

This is more evident in Fig. 18: as the CBL deepens, so does the layer of MSC; the onset and peak times of MSC at levels above the surface lag compared to those of surface MSC. The resulting maximum  $w_{MS}$  at a scale of  $900 \text{ km}^2$  is  $8 \text{ cm s}^{-1}$ , at 1700 UTC at a height close to the mountain-top level. This is insignificant compared to typical short-lived convective drafts in the CBL, but significant in terms of the long-lived solenoidal circulation. The level of nondivergence also deepens with CBL depth, and solenoidal divergence occurs near the CBL top, although not continuously. At least before solar noon the low-level solenoidal convergence exceeds the upper-CBL divergence so there is some net flux into the free troposphere, consistent with cumulus development starting at 1600 UTC, with cloud tops 1.5–2 km above the CBL top (Fig. 12). Note that at 1600 UTC no upper-CBL divergence exists, indicating that a substantial fraction of the solenoidal circulation is vented into the free troposphere.

A weak convergence burst occurs at 1900 UTC up to 625 hPa (i.e., above the CBL and above the cloud base; LCL  $\sim 675$  hPa). This deep convergence and the weakly

divergent surface flow (Fig. 18) are consistent with the Cu convection at a much smaller scale [section 3b(2)]. During the afternoon, the solenoidal circulation in the CBL weakens, although the CBL still deepens. The evening MSC profile evolution is similar to that on 12 July: while divergent flow develops near the surface, the flow in the residual mixed layer becomes convergent, with elevated MSC peaking just after sunset. We believe that this convergence in the residual mixed layer is due to a residual anabatic pressure gradient force [section 3a(4)]. WRF produce such elevated MSC just after sunset on most other CuPIDO days. Both evenings studied in this paper lack CAPE, even when computed using a parcel starting in the residual mixed layer, but on other, less stable days the resulting mountain-scale ascent triggers orographic deep convection, both observed and modeled, as will be shown in Part II.

#### 4) FORCING OF THE ANABATIC SURFACE FLOW

The anabatic forcing period lags 2–3 h behind the cycle of solar radiation and surface sensible heat flux, as on 12 July (Fig. 19). The anabatic forcing also lags behind the surface MSC, for all boxes. A 0–1-h lag occurs relative to the start of anabatic flow; and the peak anabatic forcing lags 1–6 h behind the peak anabatic flow. The latter lag is slightly greater than on 12 July, because the MSC is interrupted by Cu convection. The  $900 \text{ km}^2$

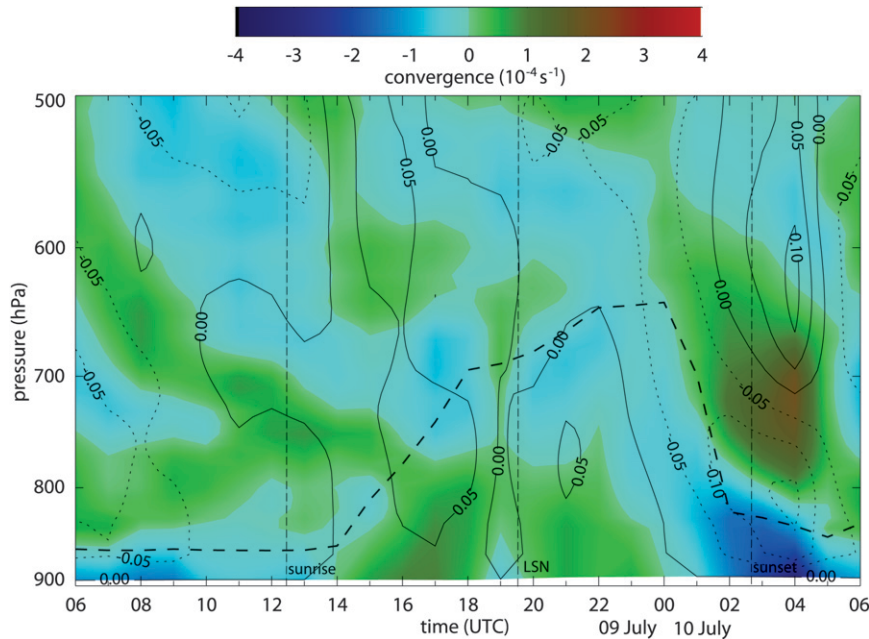


FIG. 18. As in Fig. 9, but for the 9 Jul 2006 case.

MSC peaks at 2000 UTC, close to solar noon, in the non-microphysics simulation on 9 July (not shown) (i.e., 2 h later than in the reference simulation) and also in the reference simulation on 12 July without orographic Cu (Fig. 10). Thus, the relatively early peaking of anabatic flow on 9 July is in part a moist convection feedback process. Geerts et al. (2008) point out that surface MSC peaks earlier on days with orographic thunderstorm and cold-pool development.

The diurnal cycle of the pressure gradient forcing is smoother than that of surface MSC and shows no impact

of the lightly-precipitating convection at 1900 UTC, which causes a dip in MSC in all but the largest box (Fig. 19). In fact the magnitude and phasing of the anabatic forcing is remarkably similar on 9 and 12 July, suggesting that at least relatively shallow cumulus convection has little effect on the evolution of surface pressure over the mountain. From a hydrostatic perspective, the shallow cooling by cloud shading and evaporation of rain appears to be offset by latent heating aloft. Thus, it is conceivable that convectively induced divergent surface flow undercuts convergent flow above the surface (but

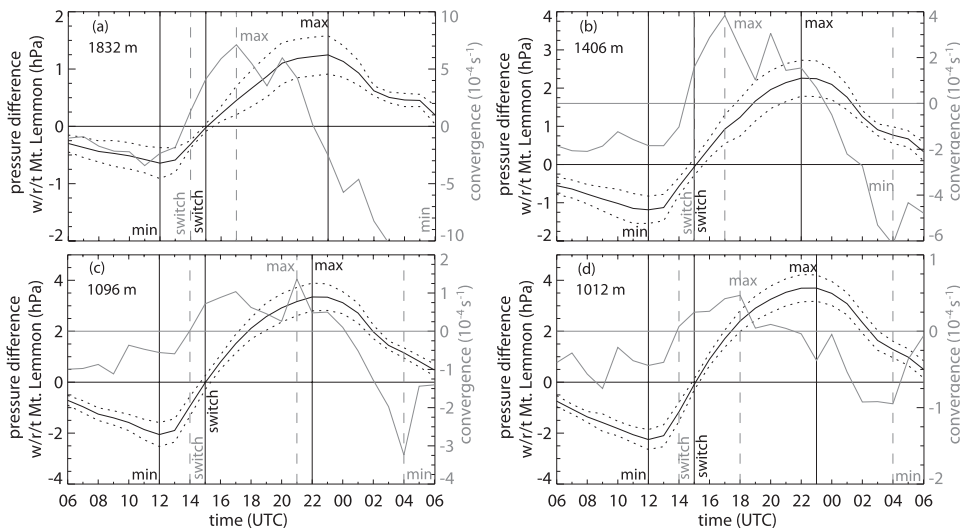


FIG. 19. As in Fig. 10, but for the 9 Jul 2006 case.

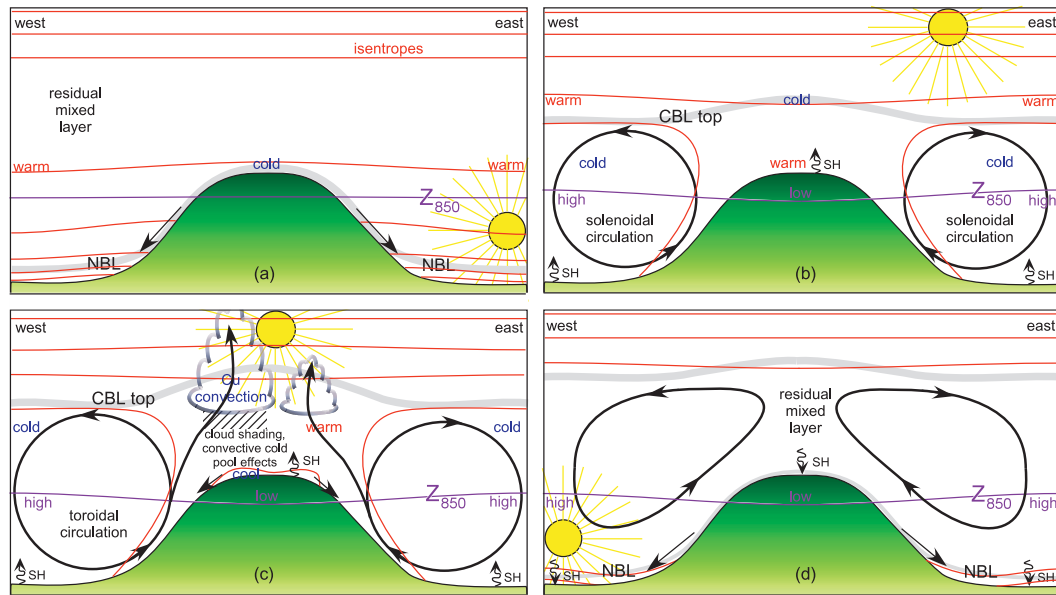


FIG. 20. Conceptual view of the diurnal evolution of a weakly capped CBL and thermally forced circulation over an isolated mountain under negligible mean wind and enough moisture for shallow to mediocre cumulus development. The horizontal (vertical) dimensions of the west–east cross section are  $\sim 50$  km ( $\sim 5$  km). The times shown are (a) near sunrise; (b) shortly before orographic cumulus development; (c) orographic cumulus phase, typically around solar noon; and (d) near sunset. Red contours are dry isentropes, purple contours indicate variations of the height of the 850 hPa surface ( $Z_{850}$ ) and thus the direction of the pressure gradient, the bold gray contour is the top of the CBL or the nocturnal boundary layer (NBL), and the black arrowed contours indicate the mean secondary circulation. The sign of the surface sensible heat (SH) flux is indicated by the squiggly arrow near the surface, pointing upward for a positive heat flux.

still within the CBL) driven by the anabatic pressure gradient. This may explain the convergence above the surface at 1900 UTC (Fig. 18). In Part II we will examine the validity of this mechanism for deeper convection.

#### 4. Discussion and conclusions

Two numerical simulation case studies are presented to study the development of the daytime CBL over a  $\sim 30$ -km-wide,  $\sim 2$ -km-high mountain during the summer in southeastern Arizona. The CBL is not well capped in either case. The case studies occurred during CuPIDO, a field campaign that provided a wealth of data around the CM for model validation. The model, WRF version 3, with a horizontal resolution of 1 km, nicely captures the observed temperature distribution, as well as mountain-scale anabatic flow development in a deep, intensely turbulent CBL. In the first case (12 July 2006), the model produces no orographic cumuli, although Cu congestus was observed over the mountain. In the second case (9 July 2006), the model produces Cu mediocris (up to 2.8 km deep) with a trace of precipitation, while in reality only Cu humilis formed over the CM. Aside from this disagreement, the WRF version 3 simulations are

remarkable accurate, as verified against surface observations and soundings, and also remarkably realistic. The differences between model and observations in terms of observed orographic cloud evolution can be attributed to differences in low-level moisture.

The two WRF case studies confirm several findings based on case study and composite observations in Geerts et al. (2008) and Demko et al. (2009). First, drainage flow transitions into anabatic, convergent flow shortly after sunrise, peaks close to solar noon, and decays throughout the afternoon. Second, cold pools associated with orographic cumulus convection can temporarily overwhelm this convergence around the mountain. The diurnal trend of surface MSC is rather bell shaped on the cloud-free day (12 July), but it shows two maxima straddling the period of most active cumulus convection and light precipitation over the mountain on the other day (9 July). And third, MSC in the lower troposphere is forced by a hydrostatic perturbation pressure gradient force toward the mountain. This forcing is solenoidal (i.e., it is due to a warm anomaly over the CM). This warm anomaly must be due to the surface sensible heat flux over elevated terrain. In the presence of a warm anomaly, the low-level convergent flow advects cold air, but the

resulting local cooling is offset by the sensible heat flux over the mountain surface. Close to the steep sloping terrain, strong sensible heating occurs from the surface, resulting in upslope flow driven by buoyancy rather than an hydrostatic pressure gradient. This is similar to nocturnal katabatic flow, which is driven by near-surface negative buoyancy rather than a divergent hydrostatic pressure gradient force.

The dynamically consistent, continuous, 3D WRF output allows some new insights (Fig. 20) beyond the observations, which are mostly limited to the surface. First, divergent flow develops in the upper CBL, and the level of nondivergence (between the low-level inflow and the upper-CBL outflow) rises as the CBL deepens over the mountain. This solenoidal circulation is relatively weak and can only be teased out through the averaging of flow dominated by transient convective thermals. It can easily be shifted downwind of the mountain crest and be tilted by ambient wind shear. The ascending branch of the circulation is composed of more tightly packed CBL thermals whereas weak net subsidence exists over the adjacent valleys.

Second, if moist convection develops above the CBL, typically close to solar noon, then not only is the surface MSC suppressed by cloud shading of the ground and by convective downdraft processes, but also is the mountain-scale upper-CBL divergence measurably reduced, as a mountain-scale updraft (materialized in much smaller cumulus towers) carries CBL air into the free troposphere (Fig. 20c). The interaction between the CBL circulation and orographic deep convection is explored further in Part II.

Third, the daytime warm anomaly over the high terrain is rather shallow, and does not extend over the depth of the CBL, which bulges above the mountain. A weak cool anomaly exists in the mature upper CBL over the mountain (Fig. 20b). This cool anomaly is hydrostatically consistent with a positive geopotential height anomaly near 600 hPa at 2100 UTC in both cases (not shown); this high enables divergent flow in the upper CBL. The WRF output also provides an explanation for the apparent inconsistency that the diurnal variation of the anabatic forcing period [defined in section 3a(1)] lags the MSC at the surface, as observed in Geerts et al. (2008) and confirmed by the two WRF case studies. In both cases anabatic pressure gradient forcing continues until a few hours after sunset, because of the residual heat in the CBL over the mountain, yet the surface flow around the mountain tends to become divergent a few hours before sunset, as the surface net radiation becomes negative (Fig. 20d). The explanation is that the drainage flow is quite shallow initially, and that convergent flow forced by the anabatic pressure gradient

continues above the shallow stable layer. This vespereal convergent flow, possibly enhanced as it is decoupled from the surface, may trigger deep convection over the mountain. This will be explored further in Part II.

*Acknowledgments.* CuPIDO was funded by National Science Foundation (NSF) Grant ATM-0444254 and by NSF facility deployment funds. The cloud-top chronology was kindly provided by Joseph A. Zehnder.

#### REFERENCES

- Banta, R. M., 1984: Daytime boundary-layer evolution over mountainous terrain. Part I: Observations of the dry circulations. *Mon. Wea. Rev.*, **112**, 340–356.
- , and C. L. B. Schaaf, 1987: Thunderstorm genesis zones in the Colorado Rocky Mountains as determined by traceback of geosynchronous satellite images. *Mon. Wea. Rev.*, **115**, 463–476.
- Crook, N. A., and D. F. Tucker, 2005: Flow over heated terrain. Part I: Linear theory and idealized numerical simulations. *Mon. Wea. Rev.*, **133**, 2552–2564.
- Damiani, R., and Coauthors, 2008: Cumulus Photogrammetric, In-situ and Doppler Observations: The CuPIDO 2006 experiment. *Bull. Amer. Meteor. Soc.*, **89**, 57–73.
- Davis, C. A., K. W. Manning, R. E. Carbone, S. B. Trier, and J. D. Tuttle, 2003: Coherence of warm-season continental rainfall in numerical weather prediction models. *Mon. Wea. Rev.*, **131**, 2667–2679.
- Demko, J. C., B. Geerts, Q. Miao, and J. Zehnder, 2009: Boundary layer energy transport and cumulus development over a heated mountain: An observational study. *Mon. Wea. Rev.*, **137**, 447–468.
- De Wekker, S. F. J., 2008: Observational and numerical evidence of depressed convective boundary layer heights near a mountain base. *J. Appl. Meteor. Climatol.*, **47**, 1017–1026.
- , S. Zhong, J. D. Fast, and C. D. Whiteman, 1998: A numerical study of the thermally driven plain-to-basin wind over idealized basin topographies. *J. Appl. Meteor.*, **37**, 606–622.
- Fujita, T., K. A. Styber, and R. A. Brown, 1962: On the meso-meteorological field studies near Flagstaff, Arizona. *J. Appl. Meteor.*, **1**, 26–42.
- Garrett, A. J., 1980: Orographic cloud over the eastern slopes of Mauna Loa Volcano, Hawaii, related to insolation and wind. *Mon. Wea. Rev.*, **108**, 931–941.
- Geerts, B., Q. Miao, and J. C. Demko, 2008: Pressure perturbations and upslope flow over a heated, isolated mountain. *Mon. Wea. Rev.*, **136**, 4272–4288.
- Hernández, E., J. de las Parras, I. Martín, A. Rúa, and L. Gimeno, 1998: A field case study and numerical simulation of mountain flows with weak ambient winds. *J. Appl. Meteor.*, **37**, 623–637.
- Kimura, F., and T. Kuwagata, 1993: Thermally induced wind passing from plain to basin over a mountain range. *J. Appl. Meteor.*, **32**, 1538–1547.
- Klemp, J. B., W. C. Skamarock, and O. Fuhrer, 2003: Numerical consistency of metric terms in terrain-following coordinates. *Mon. Wea. Rev.*, **131**, 1229–1239.
- Koch, S. E., F. Zhang, M. L. Kaplan, Y. L. Lin, R. Weglarz, and C. M. Trexler, 2001: Numerical simulations of a gravity wave event over CCOPE. Part III: The role of a mountain-plains solenoid in the generation of the second wave episode. *Mon. Wea. Rev.*, **129**, 909–933.

- Lin, Y. L., R. D. Farley, and H. D. Orville, 1983: Bulk parameterization of the snow field in a cloud model. *J. Climate Appl. Meteor.*, **22**, 1065–1092.
- Orville, H. D., 1964: On mountain upslope winds. *J. Atmos. Sci.*, **21**, 622–633.
- Paegle, J., and D. W. McLawhorn, 1983: Numerical modeling of diurnal convergence oscillations above sloping terrain. *Mon. Wea. Rev.*, **111**, 67–85.
- Reisner, J. M., and P. K. Smolarkiewicz, 1994: Thermally forced low Froude number flow past three-dimensional obstacles. *J. Atmos. Sci.*, **51**, 117–133.
- Trentmann, J., and Coauthors, 2009: Multi-model simulations of a convective situation in low-mountain terrain in central Europe. *Meteor. Atmos. Phys.*, **103**, 95–103, doi:10.1007/s00703-008-0323-6.
- Tucker, D. F., and N. A. Crook, 2005: Flow over heated terrain. Part II: Generation of convective precipitation. *Mon. Wea. Rev.*, **133**, 2565–2582.
- Vergeiner, I., and E. Dreiseitl, 1987: Valley winds and slope winds: Observations and elementary thoughts. *Meteor. Atmos. Phys.*, **36**, 264–268.
- Whiteman, C. D., 2000: *Mountain Meteorology: Fundamentals and Applications*. Oxford University Press, 376 pp.
- Yuan, H., S. L. Mullen, X. Gao, S. Sorooshian, J. Du, and H. M. H. Juang, 2007: Short-range probabilistic quantitative precipitation forecasts over the Southwest United States by the RSM Ensemble System. *Mon. Wea. Rev.*, **135**, 1685–1698.
- Zehnder, J. A., J. Hu, and A. Razdan, 2007: A stereo photogrammetric technique applied to orographic convection. *Mon. Wea. Rev.*, **135**, 2265–2277.
- Zhang, F., and S. E. Koch, 2000: Numerical simulations of a gravity wave event over CCOPE. Part II: Waves generated by an orographic density current. *Mon. Wea. Rev.*, **128**, 2777–2796.